Temperature-Induced Revolving Effect of Electronic Flow in Asymmetric Double-Barrier Semiconductor Heterostructures

Céline Belabbas,[1] Adeline Crépieux,[2] Nicolas Cavassilas,[1] Fabienne Michelini,[1] Xiangyu Zhu,[3] Chloé Salhani,[3,4] Guéric Etesse,[1] Kazuhiko Hirakawa,[3,4,5,*] and Marc Bescond[1,3,†]

[1] *Faculté des Sciences de Saint Jérôme, IM2NP, UMR CNRS 7334, Aix-Marseille Université, Case 142, 13397 Marseille Cedex 20, France*
[2] *Aix Marseille Univ, Université de Toulon, CNRS, CPT, Marseille, France*
[3] *Institute of Industrial Science, University of Tokyo, 4-6-1 Komaba, Meguro-ku, Tokyo 153-8505, Japan*
[4] *LIMMS-CNRS, IRL 2820, 4-6-1 Komaba, Meguro-ku, Tokyo 153-8505, Japan*
[5] *Institute for Nano Quantum Information Electronics, University of Tokyo, 4-6-1 Komaba, Meguro-ku, Tokyo 153-8505, Japan*

(Received 4 January 2023; revised 5 June 2023; accepted 7 July 2023; published 25 July 2023)

We theoretically report a remarkable revolving effect of electron flow when applying a lattice temperature gradient across an asymmetric double-barrier heterostructure. Depending on whether the lattice temperature increases or decreases, we demonstrate that electrons respectively absorb or emit a phonon and subsequently go back to the reservoir from which they have been injected. Our simulation code, which self-consistently solves the nonequilibrium Green's function framework and the heat equation, is capable of calculating the electron temperature and electrochemical potential inside the device. By investigating those nonequilibrium thermodynamic quantities, we show that the revolving effect is due to the sign inversion of the local electron distribution. In particular, simulation results evidenced a variation of the electrochemical potential inside the device to compensate the temperature gradient, and to maintain the electrostatic neutrality in the access regions. Finally, we propose an analytic model which provides an intuitive picture of the effect, and discuss the possibility to use such behavior in the new context of heat management in nanostructures.

DOI: 10.1103/PhysRevApplied.20.014056

I. INTRODUCTION

Thermoelectric technology consists in converting heat into electricity or vice versa. It is a solid-state heat-engine solution whose devices present the advantages of high reliability, small size, and no sensitivity to vibrations. As such, they are very promising candidates to contribute to energy sustainability in a period of severe shortage. Thermoelectric devices have therefore attracted increasing interest during the last decade [1,2]. Those devices are based on diffusive phonon and electron transport, and operate in the close-to-equilibrium regime, where their produced power is obviously limited. The scenario is significantly different in nanostructures where carrier transport can be assumed to be strongly ballistic. In this nonequilibrium regime, the electron temperature may differ significantly from the lattice one, raising the opportunity to obtain devices with better performance than conventional thermoelectric structures, in particular due to energy filtering [3].

However, in semiconductor nanostructures, the interplay between potential barrier height, transport properties, and electron or lattice temperatures is still unclear. Therefore, extensive theoretical investigations of thermoelectric nanodevices are needed. In order to capture the key aspects of the physics, we use the quantum nonequilibrium Green's function (NEGF) method. Our quantum transport code takes into account the thermal effects by self-consistently coupling the electron transport equations expressed within the NEGF formalism with the heat equation [4,5]. We also use the virtual probe concept to calculate the electron temperature and electrochemical potential inside the device [6,7].

We will focus on double-barrier asymmetric heterostructures since we recently demonstrated that such devices can efficiently act on both the electronic and phononic baths' refrigeration when a bias is applied between the emitter and collector contacts [8]. We consider the device shown in Fig. 1. It illustrates the band diagram of the asymmetric double-barrier heterostructure

*hirakawa@iis.u-tokyo.ac.jp
†marc.bescond@cnrs.fr

 © 2023 American Physical Society

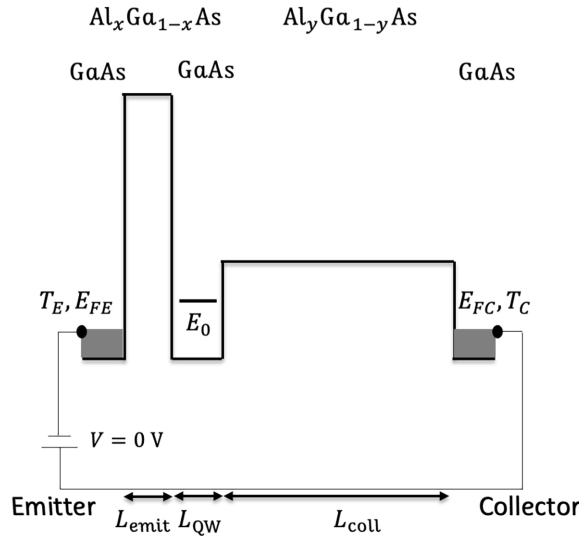

FIG. 1. Sketch of the considered asymmetric double-barrier heterostructure. Here, L_{emit}, L_{QW}, and L_{coll} refer to the thicknesses of the emitter barrier, the quantum well, and the collector barrier, respectively; E_0 is the QW state; while E_{FE} (T_E) and E_{FC} (T_C) are the Fermi levels (temperatures) of the emitter and collector, respectively. For all the considered devices, doping in the emitter and the collector is 10^{18} cm^{-3}, $L_{\mathrm{emit}} = L_{\mathrm{QW}} = 5$ nm, and $L_{\mathrm{coll}} = 100$ nm. The aluminum concentrations in the emitter and collector barriers are x and y, respectively. The value $x = 0.45$ corresponds to a barrier height of 0.38 eV, while the value $y = 0.1$ corresponds to a barrier height of 0.075 eV.

which couples "tunnel injection" and "thermionic extraction." When applying a bias, "cold" electrons are injected from the emitter into the GaAs quantum well (QW) via a resonant tunneling effect through a thin potential barrier (labeled as "emitter barrier"). The role of the emitter barrier is to filter injected electrons and to concentrate the cooling in the QW. "Hot" electrons are removed from the QW through a thermionic process above the thick (Al, Ga)As alloy (labeled as "collector barrier"), extracting energy from the lattice via phonon absorption. Electrons are then relaxed in the collector by emitting phonons. As a result, the QW cools and the collector heats. We showed that the electron bath in the QW was also refrigerated thanks to the evaporative cooling effect. When applying a bias, hot electrons are extracted above the thick collector barrier and the remaining low-energy ones rethermalize in the QW at a lower temperature [8,9].

In this work, we focus on the opposite effect, i.e., when a temperature gradient is applied between the collector and the emitter, and we study the induced electrical current properties. We demonstrate that electrons are subject to an unexpected revolving effect, for which carriers coming from the collector (emitter) are reflected back to the contact at a lower (higher) energy when reaching the collector (emitter) barrier. For energies below 50 meV, this generates an electron flow which goes against the temperature gradient. This revolving effect is accompanied by phonon emission (absorption), and it is here interpreted by a thermodynamic analysis of the variations of the local electrochemical potential and temperature. Indeed, we show that the difference of the Fermi-Dirac distribution between two consecutive planes depicts a sign inversion at an energy of 50 meV, in agreement with the current spectral features. We note that the role of the quantum well is less obvious in this operating configuration and will require additional investigations, for instance, to assess the impact on the Seebeck thermodynamic factor compared to a device without a quantum well.

The paper is organized as follows. Section II describes the electronic quantum transport, heat transport model, and calculation of thermodynamic quantities based on the virtual probe approach. In Sec. III, we investigate the revolving effect and emphasize the role of the nonequilibrium electron temperature and electrochemical potential inside the structure. From these results, we propose a compact model which confirms this phenomenon and discuss its possible applications for heat management in nanostructures. Finally, Sec. IV draws our concluding remarks.

II. THEORETICAL APPROACH

In order to theoretically study such a quantum device, we couple both electron and phonon transport. As the approach has already been described in previous studies [4,5,9], we therefore briefly recall below the milestones of the theory and the computational implementation.

A. Transport of electron and heat

Electron transport is described via the NEGF quantum formalism [10,11]. Transport equations are expressed within the effective-mass approximation to implement a quantum simulator along the heterostructure growth direction (x). The single-band effective-mass Hamiltonian describes the Γ valley of the conduction band of the III-V semiconductors. In the following, we summarize the main features of the NEGF approach in matrix notation.

We first define the retarded Green's function at the energy E for each transverse mode k_t,

$$G^r_{k_t} = [(E - V)I - H_{k_t} - \Sigma^r_{L,k_t} - \Sigma^r_{R,k_t} - \Sigma^r_{S,k_t}]^{-1}, \quad (1)$$

where I is the identity matrix, H_{k_t} represents the effective-mass Hamiltonian for k_t, and V is the electrostatic potential energy. Assuming cylindrical symmetry, the transverse mode k_t is given by $k_t = n_{k_t} \times 2\pi/L_t$, where $L_t = 80$ nm is the cylinder diameter and n_{k_t} is an integer indexing the transverse modes, whose degeneracy is equal to $\pi(2n_{k_t} + 1)$ [12]. As such, the structure is assumed to be translationally invariant in the perpendicular plane with respect to the transport direction. The choice of $L_t = 80$ is large enough

to obtain a refined mesh of transverse wave vector. This approach has led to successful comparison of simulation results and experimental measurements [8]. Finally, above, Σ_L^r (Σ_R^r) and Σ_S^r are the retarded self-energies for the left (right) semi-infinite device contacts [13] and scattering mechanisms, respectively.

From the retarded Green's function, the lesser (greater) Green's functions are then obtained as

$$G_{k_t}^{\lessgtr} = G_{k_t}^r(\Sigma_{L,k_t}^{\lessgtr} + \Sigma_{R,k_t}^{\lessgtr} + \Sigma_{S,k_t}^{\lessgtr})G_{k_t}^{r\dagger}, \tag{2}$$

where $\Sigma^{\lessgtr}$ are the lesser (greater) self-energies, related to their retarded counterpart by

$$\Sigma^r = \tfrac{1}{2}[\Sigma^> - \Sigma^<]. \tag{3}$$

Only acoustic- and polar-optical-phonon [14] interactions are considered, since non-polar-optical phonons turn out to be negligible in the semiconductors considered in this work [15,16]. Interactions with acoustic ones (AC) are assumed elastic at room temperature [4], while polar-optical phonons (POP) have an energy $\hbar\omega_{\mathrm{LO}} = 35$ meV. Interaction self-energies are calculated within the self-consistent Born approximation (SCBA) [17–19].

Interactions with polar-optical phonons are here assumed to be local and we then consider only the diagonal part of the matrix self-energies. We indeed proposed a diagonal expression of the POP scattering self-energy $\Sigma_{\mathrm{POP},k_t}^{\lessgtr}$ for phonons with longitudinal frequency. The latter approach is based on a scaling factor which takes into account the diagonal approximation and which is obtained within a physically based analytical model [14].

For a given wave vector k_t, it can be shown that

$$\begin{aligned}\Sigma_{\mathrm{POP},k_t}^{\lessgtr}(j,j,E) &= \frac{\lambda M^2}{2\pi S}\sum_{k_t'}[(n_L(j)+1)G_{k_t'}^{\lessgtr}(j,j,E\pm\hbar\omega_{\mathrm{LO}}) \\ &\quad + n_L(j)G_{k_t'}^{\lessgtr}(j,j,E\mp\hbar\omega_{\mathrm{LO}})] \\ &\quad \times\int_{\pi/L_t}^{\pi}\frac{\pi(2n_{k_t'}+1)}{\sqrt{(k_t-k_t'\cos\theta)^2+(k_t'\sin\theta)^2}}\,d\theta,\end{aligned} \tag{4}$$

with $n_L(j) = (e^{\hbar\omega_{\mathrm{LO}}/(k_B T_{\mathrm{POP}}(j))} - 1)^{-1}$, $M^2 = 2\pi\hbar\omega_{\mathrm{LO}} e^2(1/\epsilon_\infty - 1/\epsilon_0)$, θ is the angle between k_t and k_t', $S = \pi L_t^2$, and $\hbar\omega_{\mathrm{LO}} = 35$ meV. The index j indicates the x position along the discretized domain, while M is the Fröhlich factor in which ϵ_0 and ϵ_∞ represent the static and high-frequency dielectric permittivities, respectively. Finally, λ is a scaling factor which takes into account the diagonal approximation. The value $\lambda = 8$ used in this paper has been obtained within the comprehensive and physically based analytical model proposed in Ref. [14].

Interface-roughness scattering is also assumed to be negligible with respect to polar-optical-phonon scattering. On that point, we can mention the work of Lake *et al.* [20], who showed that polar-optical-phonon scattering is significantly larger than the interface-roughness contribution in GaAs/AlAs resonant tunneling diodes. Moreover, this interface treatment provided an excellent agreement between modeling and experimental comparisons on both the current-voltage characteristics and the electron temperatures [please see Figs. 2(a) and 3(d), respectively, of Ref. [8]].

The total scattering SCBA self-energy $\Sigma_{S,k_t}^{\lessgtr}$ for a given mode k_t can then be decomposed as

$$\Sigma_{S,k_t}^{\lessgtr} = \Sigma_{AC,k_t}^{\lessgtr} + \Sigma_{POP,k_t}^{\lessgtr}. \tag{5}$$

Once the lesser (greater) Green's function $G_{k_t}^{\lessgtr}$ of each mode k_t is determined, the electron density can be calculated [17]:

$$n_j = -2\times\frac{i}{2\pi}\sum_{k_t}\pi(2n_{k_t}+1)\int_{-\infty}^{+\infty}G_{k_t}^<(j,j;E)\,dE, \tag{6}$$

$$= -i\int_{-\infty}^{+\infty}G^<(j,j;E)\,dE. \tag{7}$$

Here $G^<(j,j;E) = \sum_{k_t}(2n_{k_t}+1)G_{k_t}^<(j,j;E)$ and the index j indicates the x position along the discretized domain. The carrier current density flowing from position j to $j+1$ is calculated from the off-diagonal elements $(j,j+1)$ of $G_{k_t}^<(i,j;E)$ as

$$\begin{aligned}J_{j\to j+1} &= \int_{-\infty}^{+\infty}dE\,\frac{e}{\hbar}\sum_{k_t}\frac{(2n_{k_t}+1)}{S} \\ &\quad\times[H_{j,j+1}G_{k_t}^<(j+1,j;E) \\ &\quad - G_{k_t}^<(j,j+1;E)H_{j+1,j}] \\ &= \int_{-\infty}^{+\infty}\mathcal{J}_{j\to j+1}(E)\,dE,\end{aligned} \tag{8}$$

where $H_{j,j+1}$ corresponds to the nearest-neighbor hopping term in the discretized tight-binding-like Hamiltonian and $\mathcal{J}_{j\to j+1}(E)$ is the current density spectrum (in $\mathrm{A\,m^{-2}\,eV^{-1}}$). From Eq. (8) we can deduce the corresponding electronic energy current [21]:

$$J_{j\to j+1}^E = \int_{-\infty}^{+\infty}E\,\mathcal{J}_{j\to j+1}(E)\,dE \tag{9}$$

$$= \int_{-\infty}^{+\infty}\mathcal{J}_{j\to j+1}^{\mathcal{T}}(E)dE. \tag{10}$$

Taking the derivative of $\mathcal{J}^{\mathcal{T}}$, we can obtain the power density spectrum exchanged between the electron and phonon baths (in $\mathrm{m}^{-3}\,\mathrm{s}^{-1}$):

$$J^{\mathcal{T}}_{j\to j+1}(E) = -\nabla_j \mathcal{J}^{\mathcal{T}}_{j\to j+1}(E). \tag{11}$$

In practice, the set of equations (1)–(5) is solved self-consistently using a recursive algorithm [13,22] until the criteria of convergence for both electron density and carrier current density are reached. The potential energy V is self-consistently determined by nonlinearly coupling the transport equations (1)–(5) with the Poisson equation through the electron density. In all the study, band offsets are calculated based on the values reported in Ref. [23]. The other parameters used in the NEGF code are reported in Table I.

Equation (11) directly determines the energy transferred between the electron bath and the lattice, establishing the coupling between the heat equation and electron transport equations. The one-dimensional heat equation along the x direction (which determines the lattice temperature) is then iteratively solved together with the transport equations and the Poisson equation, until a global self-consistency is achieved. This approach has been precisely described in Ref. [4,5].

B. Nonequilibrium thermodynamic parameters

Since the device operates in a strongly nonequilibrium regime, the temperature of the electrons can significantly differ from that of its lattice counterpart. In this section, we detail how the local electronic temperature and electrochemical potential are estimated based on the virtual probe approach. Within this method, the local thermodynamic parameters are those canceling the particle and energy currents between a floating probe and a point of the device. The probe is then in local thermodynamic equilibrium with the nonequilibrium structure. Stafford and co-workers [6,7,25] showed that the temperature and electrochemical potential determined within this approach are physically consistent, as they are unique and fulfill the four laws of thermodynamics.

We then consider a thermoelectric probe at the position j along the x axis defined by the following self-energy (similar to the Büttiker probes [26–28]):

$$\Sigma^{>}(j;E) = -i[1 - f_{\mathrm{FD}}(E,\mu_j,T^e_j)]D(j;E)\nu_{\mathrm{coup}}, \tag{12}$$

$$\Sigma^{<}(j;E) = i f_{\mathrm{FD}}(E,\mu_j,T^e_j)D(j;E)\nu_{\mathrm{coup}}. \tag{13}$$

Here f_{FD} is the Fermi-Dirac distribution of the electrons in the probe; μ_j and T^e_j, respectively, are the local electrochemical potential and electronic temperature at position j; $D(j;E) = i([G^{>}(j,j;E) - G^{<}(j,j;E)]/2\pi)$ is the local density of states of the probe (taken equal to that of the device); and ν_{coup} is the energy-independent coupling strength between the probe and the system. The exact value of ν_{coup} is irrelevant, as it will cancel out in the following computations.

By enforcing the simultaneous cancelation of the electron charge and energy currents at each point j between the device and the probe, we obtain a system of two coupled nonlinear equations in the unknowns μ_j and T^e_j:

$$\Delta J(j) = \int_{-\infty}^{+\infty} \Sigma^{>}(j;E)G^{<}(j,j;E)\,dE - \int_{-\infty}^{+\infty} G^{>}(j,j;E)\Sigma^{<}(j;E)\,dE = 0, \tag{14}$$

$$\Delta J^E(j) = \int_{-\infty}^{+\infty} E\Sigma^{>}(j;E)G^{<}(j,j;E)\,dE - \int_{-\infty}^{+\infty} EG^{>}(j,j;E)\Sigma^{<}(j;E)\,dE = 0. \tag{15}$$

The system is iteratively solved at each position j through a Newton-Raphson algorithm [29]. These calculations are done as a postprocessing step once the self-consistent lesser and greater Green's functions of the system are obtained. The physical validity of this approach has been discussed in Sec. III.B of Ref. [9].

III. RESULTS AND DISCUSSION

A. Physical analysis

We consider the structure shown in Fig. 1 on which we applied a temperature gradient of 1 K between the collector and emitter ($T_{\mathrm{emit}} = 300$ K and $T_{\mathrm{coll}} = 301$ K) without applying a bias voltage. Figure 2(a) represents the resulting lattice temperature, which varies linearly across the structure (a constant thermal conductivity equal to 46 $\mathrm{W\,m^{-1}\,K^{-1}}$ is assumed in all the materials). Figure 2(b) shows the corresponding electron-current spectrum [$\mathcal{J}_{j\to j+1}(E)$ of Eq. (8)].

Interestingly, we can see that the current directions in the emitter and collector access regions depend on the energy. The electrons with an energy lower than 50 meV go from left to right (i.e., against the temperature gradient), while

TABLE I. Principal NEGF parameters used.

	m^*_Γ(GaAs)	m^*_Γ(AlAs)	$m^*_\Gamma(\mathrm{Al}_x\mathrm{Ga}_{1-x}\mathrm{As})$	$\hbar\omega_{\mathrm{LO}}$ (meV)	ϵ_0	ϵ_∞
	0.067	0.15	$xm^*_\Gamma(\mathrm{AlAs}) + (1-x)m^*_\Gamma(\mathrm{GaAs})$	35	12.9	10.89
Ref.	[23]	[23]	[23]	[24]	[24]	[24]

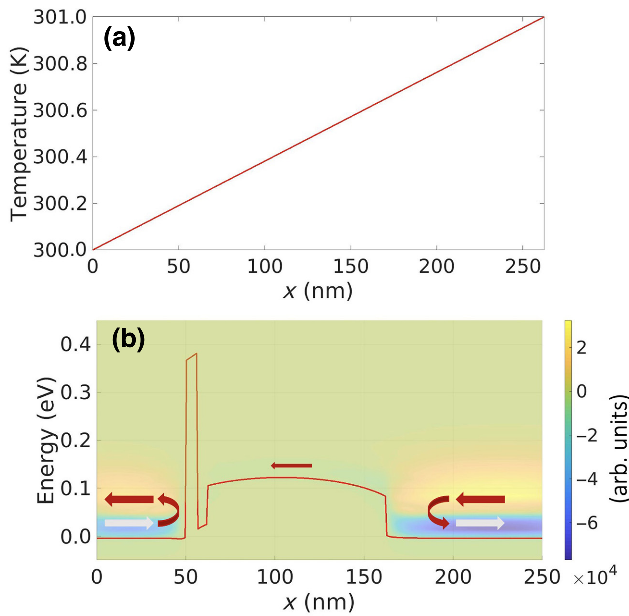

FIG. 2. (a) Lattice temperature gradient along the device shown in Fig. 1. A 1 K temperature gradient is applied between the emitter ($T_{\mathrm{emit}} = 300$ K) and collector ($T_{\mathrm{coll}} = 301$ K) reservoirs. (b) Corresponding electron-current spectrum. The solid red line represents the energy potential profile, while red and white arrows indicate the electron flow and reflection on the potential barrier. The smaller red arrow in the central region represents the total electron flow, going from right to left. No potential bias is applied ($V = 0$ V).

those with an energy above this value flow in the reverse direction, from right to left. At this stage, we would like to make two important remarks: (i) The total integrated current [Eq. (8)] is positive (equal to 2.825×10^3 A m^{-2}), which means that the total electron flow goes, as intuitively expected, from right to left, following the temperature gradient. (ii) The inversion of the electron flow for energies below 50 meV is not induced by a possible sign inversion of the difference of the Fermi-Dirac distributions of the emitter and collector reservoirs (i.e., $f_{\mathrm{FD_{coll}}} - f_{\mathrm{FD_{emit}}}$), which keeps the same sign for all the energies in the conduction band (not shown).

To shed light on this phenomenon, in Fig. 3 we represent the divergence of the energy current spectrum [Eq. (11)]. This physical quantity provides both a spectral (in energy) and a spatial analysis of the energy transfer between the electronic and phononic baths. The main energy transfers occur at the edges of the emitter and collector barriers (indicated by vertical arrows). On the emitter barrier side, we see a transfer of electrons from energies below 50 meV to energies above 50 meV, represented by an upward vertical arrow. On the collector barrier side, we observe an opposite behavior, with a transfer of electrons from energies above 50 meV downward to energies below 50 meV. The interpretation of the two electron fluxes now becomes clearer: On the emitter side, the injected electrons reaching the thin emitter barrier [white arrow of Fig. 2(b)] absorb polar-optical phonons and go back to the reservoir at higher energies [red arrow in Fig. 2(b)]. On the collector side, the injected electrons undergo the opposite phenomenon. While reaching the collector barrier [red arrow in Fig. 2(b)], most of the electrons emit polar-optical phonons and go back to the reservoir at lower energies [white arrow in Fig. 2(b)]. In both emitter and collector access regions, the flow of the electrons going from right to left (in yellow) is larger than the flow of electrons going from left to right (in blue), leading at the end to a total net current which follows the temperature gradient.

As a comparison, Fig. 4 shows the electron-current spectrum in the same device when a 0.1 V bias is applied without any temperature gradient ($T_{\mathrm{emit}} = T_{\mathrm{coll}} = 300$ K). In that configuration, the device operates like a cooling structure [5,8]. As expected, we see that the electron flow goes from the emitter region towards the collector side for all energies, following the difference in Fermi levels between the two reservoirs. In both the emitter access region and GaAs quantum well, the electrons absorb a phonon to reach the top of the collector barrier. Once they reach this latter region, they emit phonons to progressively thermalize within the collector reservoir. It is important to note that the magnitude of the current spectrum with applied bias is lower than that in the presence of a temperature gradient.

To understand the origin of the discrepancy in current spectral features when a temperature gradient or a bias voltage is applied, we calculate, based on the virtual probe approach, the electronic temperature and electrochemical potential along the structure in those two operating configurations. Figure 5(a) shows the electron temperature when a temperature gradient is applied. We see that the nonequilibrium electron temperature follows rather

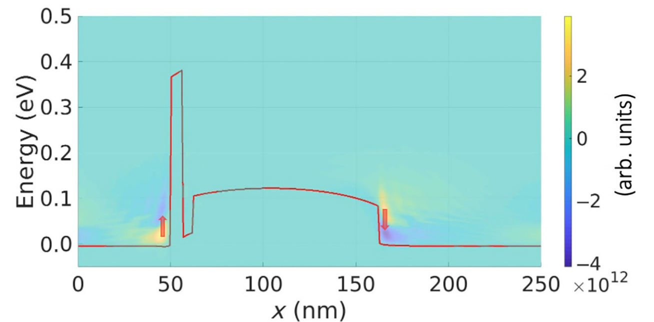

FIG. 3. Derivative of the energy current spectrum [Eq. (11)]. The yellow-colored regions represent the predominance of outgoing electrons, while blue-colored regions are those of incoming electrons. The upward-pointing arrow indicates the promotion of low-energy electrons to high-energy electrons (i.e., phonon absorption). The downward-pointing arrow indicates electron decay to lower energy (phonon emission).

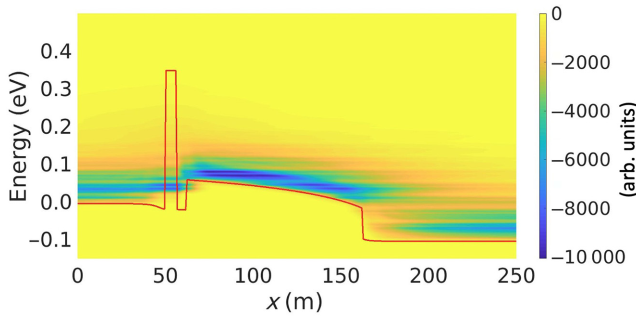

FIG. 4. Electron-current spectrum for the same structure as previously on which a potential bias of $V = 0.1$ V is applied between the emitter and collector reservoirs. No temperature gradient is considered ($T_{\rm emit} = T_{\rm coll} = 300$ K). The solid red line represents the energy potential profile. In this case, the electrons go in the same direction (i.e., from left to right) at all energies.

faithfully the variation of the lattice temperature. The small dips observed just before the emitter barrier and in the QW correspond to an evaporative cooling effect when electrons "jump" over a potential barrier by thermionic emission [9]. In contrast, the temperature peak right after the collector barrier results from the kinetic energy gain of the electrons. Finally, we should mention that the temperature does not exactly reach 300 and 301 K in the emitter and collector, respectively, since electron-phonon coupling is not strong enough to fully thermalize the electrons before entering the contacts.

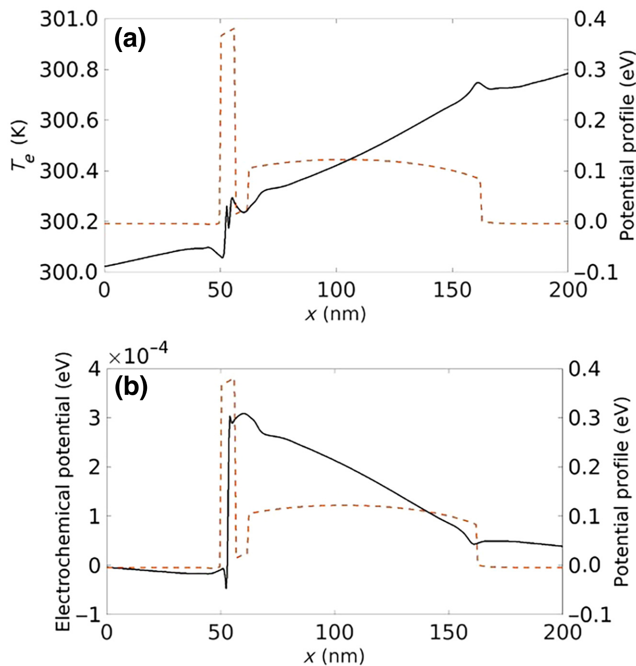

FIG. 5. (a) Nonequilibrium electron temperature along the device and (b) corresponding electrochemical potential when applying a lattice temperature gradient of 1 K and no potential bias ($V = 0$ V).

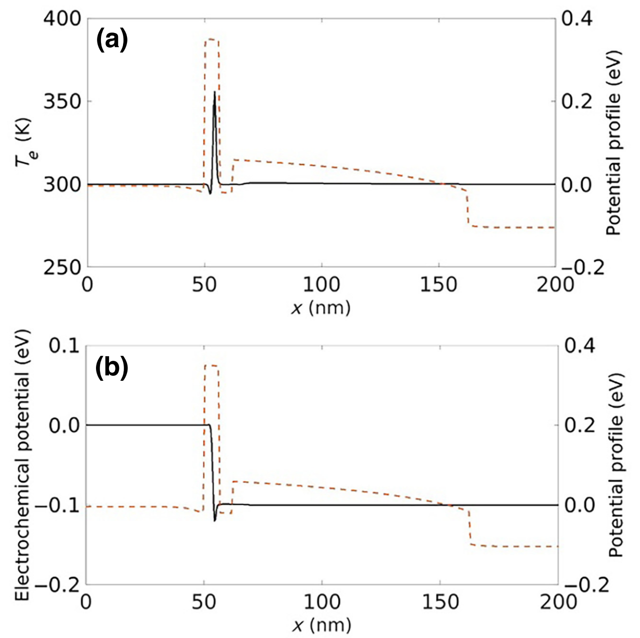

FIG. 6. (a) Nonequilibrium electron temperature along the device and (b) corresponding electrochemical potential when applying a potential bias ($V = 0.1$ V) and no temperature gradient ($T_{\rm emit} = T_{\rm coll} = 300$ K).

Figure 5(b) shows the corresponding electrochemical potential. Except for the abrupt variation in the emitter barrier, which represents the largest resistive part of the system, the electrochemical potential always decreases when going from the emitter towards the collector. This decrease can be seen as a driving force for the electrons to flow from left to right against the temperature gradient, and could be at the origin of the revolving effect observed in Fig. 2(b).

By comparison, the same thermodynamic quantities in the structure with an applied potential bias $V = 0.1$ V are plotted in Figs. 6(a) and 6(b), respectively. First, the electron temperature [Fig. 6(a)] is, in this case, almost constant along the entire structure and equal to 300 K. The small temperature decrease in the QW is due to an evaporative cooling effect [8,9]. The peak in the emitter barrier is a numerical artefact, since it is physically challenging to define an electron temperature in a tunneling region. The electrochemical potential [Fig. 6(b)] is constant in intervals. It is equal to the emitter Fermi level until the first barrier, and equal to the collector Fermi level beyond this region. The difference is, of course, equal to the total applied bias, i.e., 0.1 V. The electrochemical potential profile then drains the electrons from the emitter towards the collector, following the applied bias. We also remark that, like in Fig. 5(b), the electrochemical drop occurs in the emitter barrier since it represents the most resistive part of the structure.

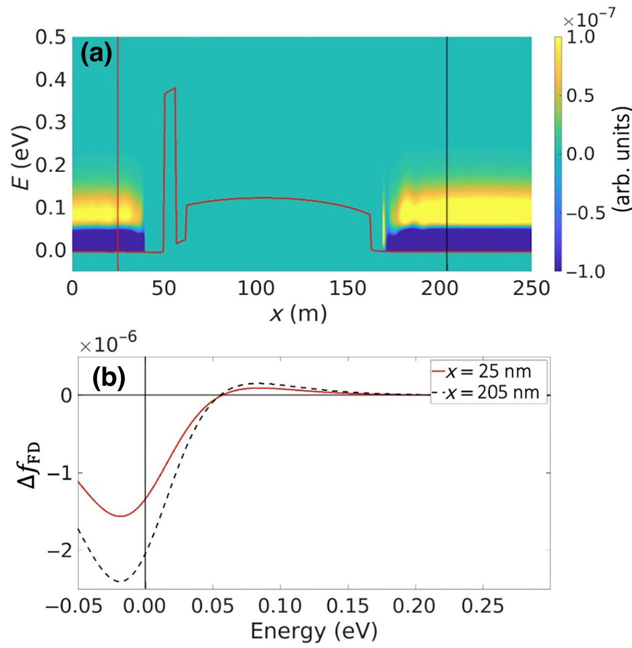

FIG. 7. (a) Difference between two consecutive planes of the Fermi-Dirac distributions calculated with the electron temperature and chemical potential shown in Figs. 5(a) and 5(b), respectively. (b) Vertical cuts of Fig. 7(a) at $x = 25$ nm (red solid line) and $x = 205$ nm (black dashed line). The vertical black solid line defines the Fermi levels of the emitter and collector (equal, since there is no applied bias).

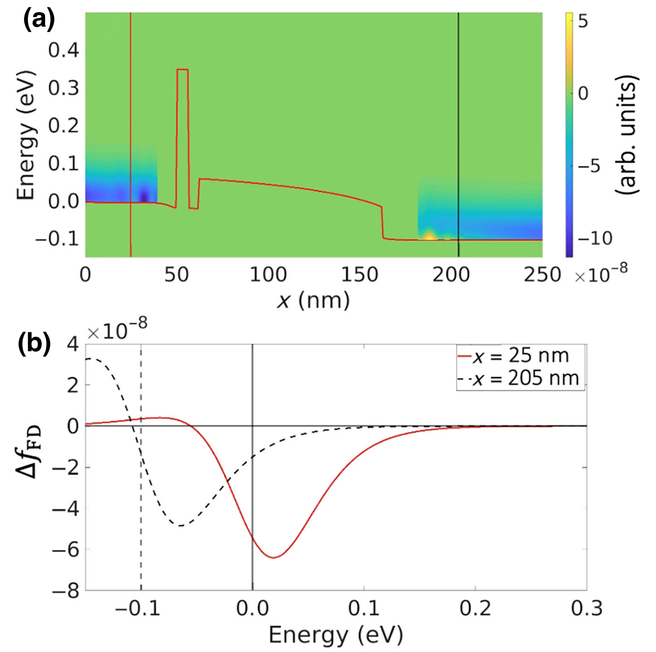

FIG. 8. (a) Difference between two consecutive planes of the Fermi-Dirac distributions calculated with the electron temperature and chemical potential shown in Figs. 6(a) and 6(b), respectively. (b) Vertical cuts of Fig. 8(a) at $x = 25$ nm (red solid line) and $x = 205$ nm (black dashed line). The vertical black solid (dashed) line defines the Fermi level of the emitter (collector) ($V = 0.1$ V).

From the previous calculations of electron temperatures and electrochemical potentials, one can calculate the local Fermi-Dirac distribution f_{FD} in each plan i of the structure. We then compute the difference of this distribution between two consecutive planes j and $j+1$ ($\Delta f_{\mathrm{FD}} = f_{FD_{j+1}} - f_{FD_j}$). The resulting distribution map is plotted in Fig. 7(a) in the case of the temperature gradient (Fig. 5). Remarkably, we see that Δf_{FD} depicts the same general feature in the leads as the current spectrum of Fig. 2(b). More precisely, there is a clear sign inversion at 50 meV above the bottom of the conduction band which corresponds exactly to the energy of the flow inversion in the current spectrum. This result indicates that the current between two consecutive planes follows the Landauer formula, with a transmission probability of unity, in which the transport is governed by the difference of the left and right distributions [10], and taking the nonequilibrium electron temperature and electrochemical potential. Figure 7(b) illustrates this behaviour by showing the vertical cuts in two planes of the emitter and collector leads, at $x = 25$ nm and $x = 205$ nm, respectively. In the two vertical cuts, Δf_{FD} is negative between 0 meV (i.e., the bottom of the conduction band) and $E = 50$ meV. The sign is reversed for higher energies.

This behavior is significantly different from that obtained with the temperature and the electrochemical potential resulting from an applied bias of 0.1 V (Fig. 6). In this case, Δf_{FD}, plotted in Fig. 8(a), shows a constant sign for all energies above the bottom of the conduction band, in clear agreement with the current spectrum of Fig. 4. This corresponds to a flow of electrons from the emitter towards the collector. The vertical cuts at $x = 25$ nm and $x = 205$ nm shown in Fig. 8(b) confirm this phenomenon. In this case, Δf_{FD} is always negative in the emitter and collector regions for energies above 0 and -0.1 eV, respectively (0.1 V is applied on the collector).

The thermodynamic analysis we have developed shows that the revolving effect originates from the variation of the electrochemical potential in the active region. This variation, which is not observed when a potential bias is applied, aims at compensating for the temperature variation and thus at maintaining a constant electron density in the access regions (equal to that of the doping). To emphasize this point, Fig. 9 shows the obtained electronic temperature and electrochemical potential when artificially modifying the interaction strength between the electrons and the polar-optical phonons. We can see that the stronger the interaction, the steeper the electron temperature, which follows the lattice temperature with a linear increase from the emitter towards the collector [Fig. 9(a)]. To compensate the faster increase of temperature and to maintain a constant electron density, the electrochemical potential

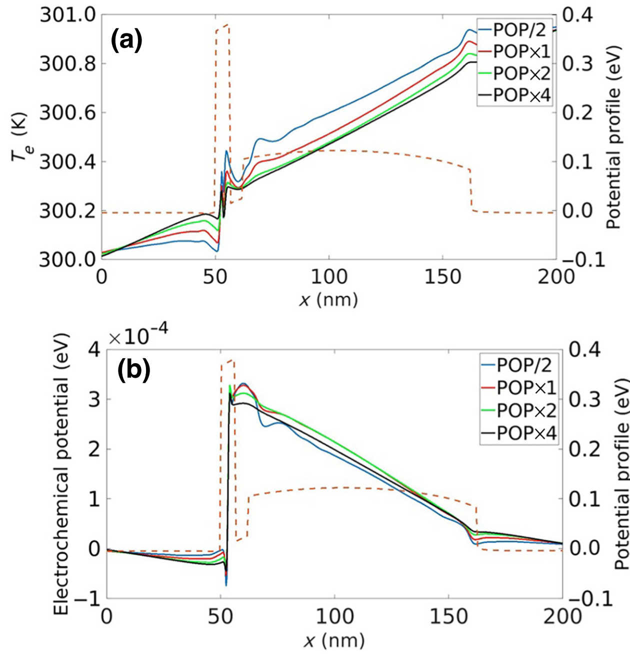

FIG. 9. (a) Electron temperature and (b) electrochemical potential along the device for four different coupling strengths with polar-optical phonons: divided by 2 (blue), standard (red), multiplied by 2 (green), and multiplied by 4 (black). The dashed line represents the potential profile. Here $T_{\mathrm{emit}} = 300$ K, $T_{\mathrm{coll}} = 301$ K, and $V = 0$ V.

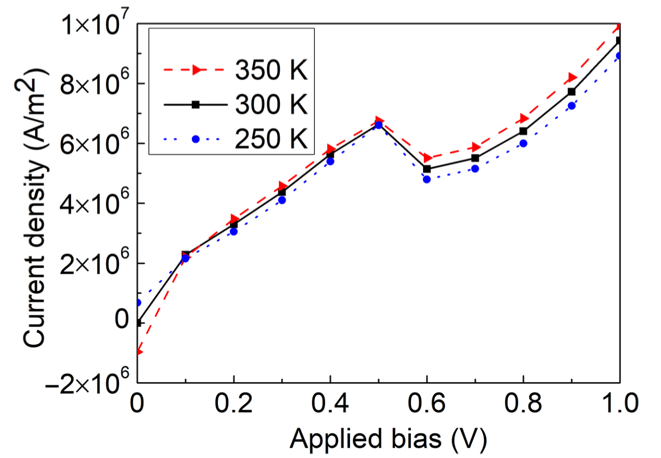

FIG. 10. Plot of $J(V)$ for three different temperature profiles: (i) with a positive 50 K gradient, i.e., $T_{\mathrm{emit}} = 300$ K, $T_{\mathrm{coll}} = 350$ K (triangles); (ii) without gradient, where the lattice temperature equals 300 K in all the device (squares); and (iii) with a negative 50 K gradient, i.e., $T_{\mathrm{emit}} = 300$ K, $T_{\mathrm{coll}} = 250$ K (circles). We consider the structure of Fig. 1 with an aluminum concentration in the collector barrier $y = 0.2$, corresponding to a barrier height of 160 meV. This higher barrier allows one to emphasize the impact of the revolving effect on current characteristics.

shows the opposite trend, with a steeper decrease in the emitter, central, and collector regions.

We now investigate the impact of this effect on current-voltage characteristics. Figure 10 shows $J(V)$ for three different temperature profiles: (i) without gradient, i.e., where the lattice temperature is homogeneous, equal to 300 K in all the device; (ii) with a positive 50 K gradient, i.e., $T_{\mathrm{emit}} = 300$ K, $T_{\mathrm{coll}} = 350$ K; and (iii) with a negative 50 K gradient, i.e., $T_{\mathrm{emit}} = 300$ K, $T_{\mathrm{coll}} = 250$ K. At $V = 0$ V, as expected, a T_{coll} of 350 K (respectively 250 K) induces a negative (respectively positive) current density, while the case of $T_{\mathrm{coll}} = 300$ K leads to a trivial vanishing current. More interestingly, when applying bias voltage, a temperature gradient in the opposite direction to the voltage (i.e., $T_{\mathrm{coll}} = 350$ K) induces an increase in the total current density with respect to the case without a temperature gradient (i.e., $T_{\mathrm{coll}} = 300$ K). In contrast, a temperature gradient apparently favorable to the applied bias (i.e., $T_{\mathrm{coll}} = 250$ K) leads to a current density reduction. This behavior directly derives from the revolving effect.

Figure 11 indeed shows the electron-current spectra at $V = 1$ V for the three previous temperature profiles. For $T_{\mathrm{coll}} = 350$ K [Fig. 11(a)], the electrons absorb phonons when reaching the emitter barrier, increasing their average energy. This then facilitates the electron transmission across the emitter barrier, leading to an increase of the current density compared to the case where the lattice temperature is constant [see current spectrum of Fig. 11(b)]. On the other hand, for $T_{\mathrm{coll}} = 250$ K, the negative temperature gradient induces a phonon emission at the emitter barrier. This results in a decrease of the electron energy, and therefore a reduction of the total current density [Fig. 11(c)]. The revolving effect can then be experimentally evidenced by performing $J(V)$ measurements at various temperature gradients. Moreover, this may represent a relevant approach to improve the performance of electronic devices by increasing or decreasing the current density.

The key findings of this study are threefold. First, we have shown that the so-called revolving effect, obtained when applying a lattice temperature gradient along the device, was due to both electrochemical and electron-temperature variations inside the active region to maintain an electron density equal to the doping. Second, the proposed analysis demonstrates the operability of the electron temperature and electrochemical potential determined in a nonequilibrium regime on the transport properties of nanodevices operating at room temperature. It thus represents an important step forward in the field of quantum thermodynamics, where investigation of thermodynamic quantities in a nonequilibrium regime is still an open question. Third, this effect should be experimentally observed by performing $J(V)$ measurements under a temperature gradient.

B. Discussion

The revolving effect can be summarized as follows. When entering the structure via the higher-temperature

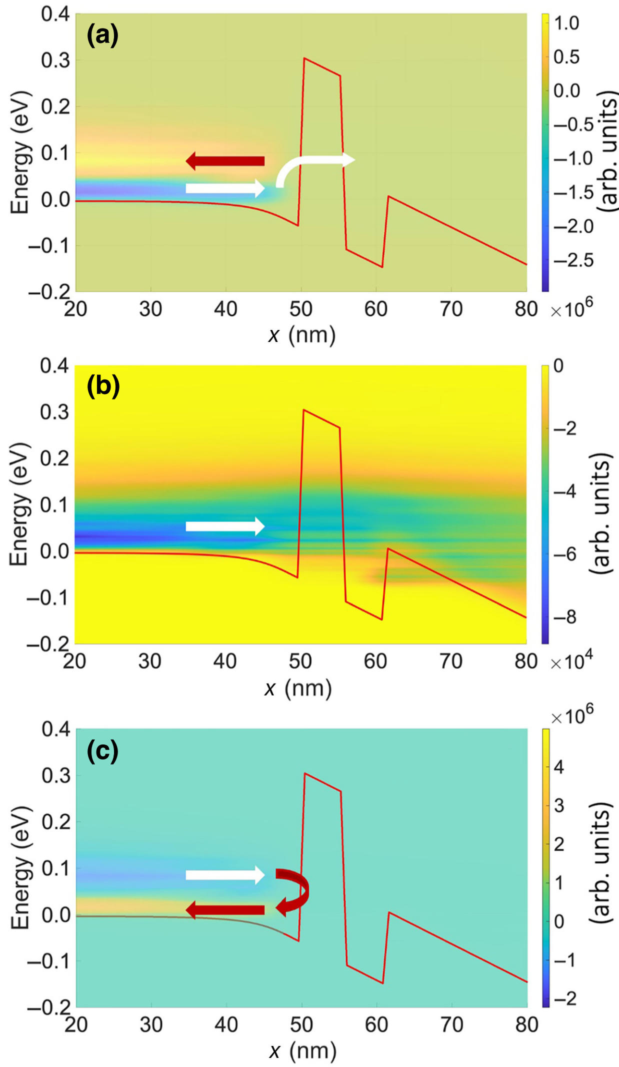

FIG. 11. Electron-current spectrum at $V = 0.1$ V for the three collector temperatures shown in Fig. 10: (a) $T_{\text{coll}} = 350$ K, (b) $T_{\text{coll}} = 300$ K, and (c) $T_{\text{coll}} = 250$ K. In all three cases, $T_{\text{emit}} = 300$ K. The solid red line represents the energy potential profile, while red and white arrows indicate the electron flow, reflection, and transmission on the potential barrier.

reservoir (i.e., collector in the present case), the electrons undergo very few interactions with phonons, since the length of the access region is much smaller than their mean free path. The decrease of the nonequilibrium electron temperature then remains smaller than that of the lattice, due to the weak interactions with the phonons in this region. At the edge of the collector barrier, the low lattice temperature induces a much smaller phonon population than that in the contact. To compensate this situation, the electrons emit phonons and are reflected back at lower energies towards the collector contact, undergoing again very few interactions with phonons (Fig. 3).

Interestingly, we show that the nonequilibrium electron temperature and electrochemical potential lead to a difference in the electron distributions between two consecutive planes with a sign inversion at 50 meV above the bottom of the conduction band [Fig. 7(a)]. This value is in good agreement with the reverse electron flow observed in the current spectrum [Fig. 2(b)]. The symmetrical phenomenon occurs on the emitter side.

We should note that the barrier edge plays the role of a scattering center. The revolving effect could also have been obtained by considering other types of scattering centers like a variation of the thermal conductivity. Figure 12 shows that we obtain a similar effect when considering a pure GaAs structure (i.e., without a potential barrier), in which the thermal conductivity is reduced to 4 W m^{-1} K^{-1} in the shaded region [see Fig. 12(a)]. Such a thermal conductivity decrease can result, for instance, from the thermal resistance associated with the interface between different layers [30]. Interestingly, Fig. 12(b) shows that the revolving effect also occurs at the borders where the thermal conductivity is modified. In that case, the effect generates a circular electron flux inside the region of low thermal conductivity.

In order to provide a more intuitive picture of this behavior, we propose a simple rate-equation model, schematically represented in Fig. 13. We consider high-energy (h) and low-energy (l) states separated by the optical-phonon energy (E_{ph}) both in a reservoir (R) and at the edge of an infinite barrier (B). This results in four states denoted $|Rh\rangle$, $|Rl\rangle$, $|Bh\rangle$, and $|Bl\rangle$. The corresponding distributions are f_{Rh},f_{Rl},f_{Bh}, and f_{Bl}. The electron fluxes between these states are defined in Fig. 13, with τ the transition rate between the reservoir and barrier edge, and M the electron-phonon coupling. The reservoir is assumed to be in equilibrium, meaning that electrons and phonons are at the same temperature T_R. The corresponding flux between $|Rh\rangle$ and $|Rl\rangle$ therefore cancels. At the barrier edge, we assume the phonons to be at temperature T_B, different from T_R. In this region, the electrons coming from the reservoir are not in equilibrium with the phonons, and then have a different temperature T_e. This results in a flux ϕ_B between $|Bl\rangle$ and $|Bh\rangle$. Flux conservation imposes that $\phi_B = \phi_l = -\phi_h$, with ϕ_l (ϕ_h) being the flux between $|Rl\rangle$ ($|Rh\rangle$) and $|Bl\rangle$ ($|Bh\rangle$). Based on this analysis, we can then compute T_e. Our results show that T_e is always between T_R and T_B. This temperature regulates the fluxes between the different states. Taking $T_R = 300$ K, $T_B = 300.5$ K, $M = \tau$, and $f_{Rh} = 10^{-4}$, we obtain $T_e = 300.32$ K. As a result, ϕ_l is positive and ϕ_h is negative, corresponding to a flux loop equivalent to the revolving effect obtained numerically. In contrast, if we consider T_B at 299.5 K, we obtain $T_e = 299.69$ K and a revolving effect in the reverse direction.

Note that such a revolving effect, while it (almost) does not transport electrons, transfers a high-energy flux from a hot area to a colder one. For instance, the device considered in Fig. 3, with a temperature gradient of only 1 K, generates an energy flux at the emitted barrier edge, due

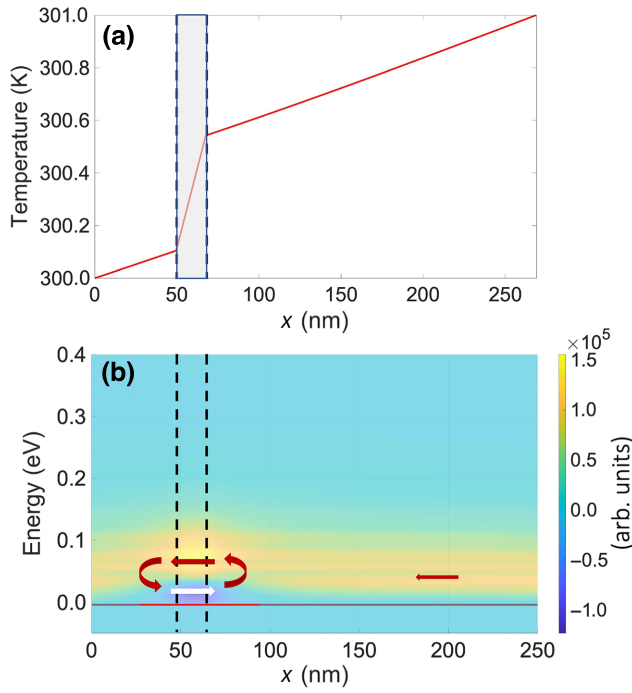

FIG. 12. (a) Lattice temperature gradient along a GaAs device of the same length as the one of Fig. 1, when considering a thermal conductivity of 4 $\mathrm{W\,m^{-1}\,K^{-1}}$ inside the shaded central region. As previously, a thermal conductivity of 46 $\mathrm{W\,m^{-1}\,K^{-1}}$ is assumed elsewhere and 1 K is applied between the emitter ($T_{\mathrm{emit}} = 300$ K) and collector ($T_{\mathrm{coll}} = 301$ K) reservoirs. (b) Corresponding electron-current spectrum. The horizontal solid red line represents the energy potential profile, while red and white arrows indicate the electron flow and reflection at the borders where the thermal conductivity varies. The smaller red arrow in the right region represents the total electron flow, going from right to left. No potential bias is applied ($V = 0$ V).

to phonon absorption, equal to 1800 $\mathrm{W\,cm^{-2}}$. In comparison, the same structure on which 1 V is applied between the emitter and collector provides a cooling power in the quantum well of 210 $\mathrm{W\,cm^{-2}}$. Such an impressive power flow could appear to be inconsistent with the fact that the lattice temperature is not modified at the edges of the emitter and collector barriers, where the power absorption or emission occurs. Nevertheless, considering the usual heat equation, the result is that a GaAs thermal conductivity of 46 $\mathrm{W\,m^{-1}\,K^{-1}}$ can drain a heat flow of more than 90 000 $\mathrm{W\,cm^{-2}}$ when a gradient temperature of 1 K is applied over 50 nm.

In order to have a significant impact of the lattice temperature, we should therefore consider devices with higher electron currents, which can be reachable by increasing the doping in the access regions, for instance. This is, however, far beyond the scope of the present work, which aims at explaining and illustrating the revolving effect. Moreover, the revolving effect can take place in any semiconductors where inelastic interactions between electrons

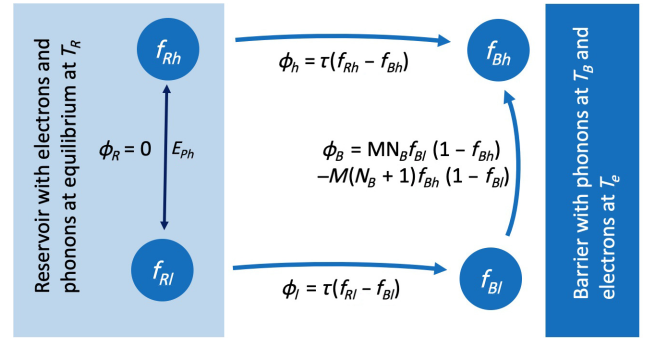

FIG. 13. Schematic representation of an analytic model of the revolving effect based on electronic flux. The left rectangle represents the reservoir at equilibrium, in which both electrons and phonons are at the same temperature, T_R. The right rectangle represents the barrier, in which the temperatures of the electrons (T_e) and phonons (T_B) can be different. On the left, f_{R_l} and f_{R_h} are the Fermi-Dirac distributions in the reservoirs of the low- and high-energy states, separated by the energy of a polar-optical phonon (E_{ph}), respectively. Similarly, on the right, f_{B_l} and f_{B_h} are the electronic distributions at the barrier edge. In the reservoir and the barrier edge, the electronic fluxes between the low and high states, due to phonon absorption or emission, are ϕ_R and ϕ_B, respectively. Also here M is the electron-phonon coupling, and N_B is the phonon's distribution at the barrier edge, given by the Bose-Einstein distribution. Finally, the fluxes between the reservoir and barrier states at high and low energy are ϕ_h and ϕ_l, respectively; and τ is the transition rate between the reservoir and the barrier states (assumed constant at low and high energies).

and optical phonons are dominant. We consider here III-V heterostructures, since their growth is technologically very well controlled, which will facilitate future experimental investigations of this effect. This could provide simple and relevant technological solutions in the semiconductor industry to electronically control the temperature in nanostructures based on a single contact.

IV. CONCLUSIONS

In this work, we report an original temperature-gradient-induced revolving effect, able to control the directional flow of electrons in a given energy interval. This effect is induced by the variation of the electrochemical potential inside the active region to compensate the electronic temperature modification and to maintain the electroneutrality in the system. As a result, the difference in the Fermi-Dirac distribution between two consecutive planes shows a sign inversion at the energy corresponding to the inversion of the flow direction in the current spectrum. Moreover, current-voltage characteristics at different temperature gradients should be a straightforward approach to experimentally verify this effect. We also propose a simple analytical model which reproduces this phenomenon and we put forward its relevance to improve heat management in electronic nanostructures. Finally, our

study demonstrates an additional validation of the virtual probe approach to determine thermodynamic properties in the strongly nonequilibrium regime.

ACKNOWLEDGMENTS

We thank A.-M. Daré, M. Lannoo, and C. Mandia for fruitful discussions on the electron-temperature calculation and the revolving effect, respectively. This work was supported by the JSPS KAKENHI (JP 19K21957), the JSPS Core-to-Core Program (A. Advanced Research Networks), the AMUTECH Master internship support, and the GELATO project from ANR (ANR-21-CE50-0017).

[1] F. Tohidi, S. Ghazanfari Holagh, and A. Chitsaz, Thermoelectric generators: A comprehensive review of characteristics and applications, Appl. Therm. Eng. **201**, 117793 (2022).

[2] N. Jaziri, A. Boughamoura, J. Müller, B. Mezghani, F. Tounsi, and M. Ismail, A comprehensive review of thermoelectric generators: Technologies and common applications, Energy Rep. **6**, 264 (2020).

[3] A. Ziabari, M. Zebarjadi, D. Vashaee, and A. Shakouri, Nanoscale solid-state cooling: A review, Rep. Prog. Phys. **79**, 095901 (2016).

[4] M. Bescond, D. Logoteta, F. Michelini, N. Cavassilas, T. Yan, A. Yangui, M. Lannoo, and K. Hirakawa, Thermionic cooling devices based on resonant-tunneling AlGaAs/GaAs heterostructure, J. Phys.: Condens. Matter **30**, 064005 (2018).

[5] M. Bescond and K. Hirakawa, High-Performance Thermionic Cooling Devices Based on Tilted-Barrier Semiconductor Heterostructures, Phys. Rev. Appl. **14**, 064022 (2020).

[6] C. A. Stafford, Local temperature of an interacting quantum system far from equilibrium, Phys. Rev. B **93**, 245403 (2016).

[7] A. Shastry and C. A. Stafford, Temperature and voltage measurement in quantum systems far from equilibrium, Phys. Rev. B **94**, 155433 (2016).

[8] A. Yangui, M. Bescond, T. Yan, N. Nagai, and K. Hirakawa, Evaporative electron cooling in asymmetric double barrier semiconductor heterostructures, Nat. Commun. **10**, 4504 (2019).

[9] M. Bescond, G. Dangoisse, X. Zhu, C. Salhani, and K. Hirakawa, Comprehensive Analysis of Electron Evaporative Cooling in Double-Barrier Semiconductor Heterostructures, Phys. Rev. Appl. **17**, 014001 (2022).

[10] S. Datta, *Electronic Transport in Mesoscopic Systems* (Cambridge University Press, Cambridge, 1995).

[11] H. Haug and A.-P. Jauho, *Quantum Kinetics in Transport and Optics of Semiconductors*, Springer Series in Solid-State Sciences Vol. 123 (Springer, Berlin, New York, 1996).

[12] N. Cavassilas, F. Michelini, and M. Bescond, Modeling of nanoscale solar cells: The Green's function formalism, J. Renew. Sustain. Energy **6**, 011203 (2014).

[13] D. K. Ferry and S. M. Goodnick, *Transport in Nanostructures* (Cambridge University Press, Cambridge, 1997).

[14] M. Moussavou, M. Lannoo, N. Cavassilas, D. Logoteta, and M. Bescond, Physically Based Diagonal Treatment of Polar Optical Phonon Self-Energy: Performance Assessment of III-V Double-Gate Transistors, Phys. Rev. Appl. **10**, 064023 (2018).

[15] A. Price and A. Martinez, Electrothermal simulations of Si and III–V nanowire field effect transistors: A non-equilibrium Green's function study, J. Appl. Phys. **12**, 6670 (2015).

[16] A. Martinez, A. Price, R. Valin, M. Aldegunde, and J. Barker, Impact of phonon scattering in Si/GaAs/InGaAs nanowires and FinFETs: a NEGF perspective, J. Comput. Electron. **15**, 1130 (2016).

[17] S. Jin, Y. J. Park, and H. S. Min, A three-dimensional simulation of quantum transport in silicon nanowire transistor in the presence of electron-phonon interactions, J. Appl. Phys. **99**, 123719 (2006).

[18] Y. Lee, M. Lannoo, N. Cavassilas, M. Luisier, and M. Bescond, Efficient quantum modeling of inelastic interactions in nanodevices, Phys. Rev. B **93**, 205411 (2016).

[19] A. Svizhenko and M. P. Anantram, Role of scattering in nanotransistors, IEEE-Trans. Electron Dev. **50**, 1459 (2003).

[20] R. Lake, G. Klimeck, R. C. Bowen, C. Fernando, T. Moise, Y. C. Kao, and M. Leng, Interface roughness, polar optical phonons, and the valley current of a resonant tunneling diode, Superlattices Microstruct. **20**, 279 (1996).

[21] R. Lake and S. Datta, Energy balance and heat exchange in mesoscopic systems, Phys. Rev. B **117**, 164501 (1992).

[22] M. Lopez-Sancho, J. Lopez-Sancho, and J. Rubio, Quick iterative scheme for the calculation of transfer matrices: Application to Mo (100), J. Phys. F: Met. **14**, 1205 (1984).

[23] I. Vurgaftman, J. R. Meyer, and L. R. Ram-Mohan, Band parameters for III–V compound semiconductors and their alloys, J. Appl. Phys. **89**, 5815 (2001).

[24] M. S. Lundstrom, *Fundamentals of Carrier Transport* (Cambridge University Press, Cambridge, 2009).

[25] J. Meair, J. P. Bergfield, C. A. Stafford, and Ph. Jacquod, Local temperature of out-of-equilibrium quantum electron systems, Phys. Rev. B **90**, 035407 (2014).

[26] M. Büttiker, Role of quantum coherence in series resistors, Phys. Rev. B **33**, 3020 (1986).

[27] G. Romano, A. Gagliardi, A. Pecchia, and A. Di Carlo, Heating and cooling mechanisms in single-molecule junctions, Phys. Rev. B **81**, 115438 (2010).

[28] R. Rhyner and M. Luisier, Atomistic modeling of coupled electron-phonon transport in nanowire transistors, Phys. Rev. B **89**, 235311 (2014).

[29] R. Venugopal, M. Paulsson, S. Goasguen, S. Datta, and M. S. Lundstrom, A simple quantum mechanical treatment of scattering in nanoscale transistors, J. Appl. Phys. **93**, 5613 (2003).

[30] M. N. Luckyanova, J. A. Johnson, A. A. Maznev, J. Garg, A. Jandl, M. T. Bulsara, E. A. Fitzgerald, K. A. Nelson, and G. Chen, Anisotropy of the thermal conductivity in GaAs/AlAs superlattices, Nano Lett. **13**, 3973 (2013).